Improved Resistive Switching Performance of Graphene Oxide Based Flexible ReRAM with HfO_x Buffer Layer

S. Maji[1], A. D. Paul[1], P. Das[1], S. Chatterjee[1], P. Chatterjee[2], V. R. Dhanak[3], A. K. Chakraborty[2,], R. Mahapatra[1*]*

[1]Department of Electronics and Communication Engineering, National Institute of Technology Durgapur, 713209, India,

[2]Department of Physics, National Institute of Technology Durgapur, 713209, India,

[3]Department of Physics and Stephenson Institute for Renewable Energy, University of Liverpool, Liverpool L69 7ZF, United Kingdom

*Email of the corresponding author: rajat.mahapatra@ece.nitdgp.ac.in, amit.chakraborty@phy.nitdgp.ac.in

Abstract

Flexible electronic devices have generated large research interest in recent years. Herein, we demonstrate a resistive random access memory (ReRAM) device fabricated on a flexible polyethylene terepthalate (PET) substrate using a bilayer of graphene oxide (GO) and HfO_x films. The physical properties of GO and HfO_x were characterized by a number of techniques such as x-ray diffraction (XRD), UV-vis absorption spectroscopy, scanning electron microscopy (SEM) and x-ray photoelectron spectroscopy (XPS). The GO/HfO_x bilayered ReRAM devices exhibited good switching behavior at low SET/RESET voltages and showed improved cell-to-cell uniformity of switching parameters compared to the devices without HfOx layer, due to the oxygen vacancies within the HfO_x film as confirmed by XPS. The switching mechanism was explained by the formation/rupture of the conductive filament through the migration-induced oxidation/reduction reaction of the oxygen vacancies at the interface of GO/HfO_x. From the I-V curve fitting, the conduction in low resistance state (LRS) was found to be governed by the Ohmic mechanism and the trap-controlled space charge limited current (SCLC) in high resistance state (HRS) was observed for both the cycles.

Keywords: ReRAM; Flexible electronics; Graphene oxide; HfO_x; resistive switching

1 Introduction

In recent years, there has been an aggressive demand of flexible electronics in electronics industry for wearable and portable applications [1-3]. For data processing and information storage applications, development of flexible non-volatile memory (NVM) is desirable [2]. The conventional flash memory which is based on metal-oxide-semiconductor field effect transistor (MOSFET) is difficult to be integrated into flexible substrates due to the severely degraded gate oxide quality at low temperature growth processes [2], [4]. Among the emerging memory technologies, resistive random access memory (ReRAM) which works on the change of resistance by an external electrical stimuli has the potential for next generation NVM application due to its simple Metal-Insulator-Metal (MIM) structure, high packaging density, high scalability, etc. [4-7]. Moreover, ReRAM fabricated at a low temperature exhibits good performance [8-10] which has attracted a great deal of attention as one of the key elements to flexible electronics.

The resistive switching effect has been explored in various materials including transitional metal oxides (TMO) [11-13], perovskite oxides [14], organic materials [15] and carbon based materials [16-19]. Among carbon based materials, graphene and its derivatives graphene oxide (GO), reduced graphene oxide (rGO) are the materials of great interest for their many interesting properties including excellent flexibility for memories and sensors applications [19-21]. GO and its composites with organic dielectrics are attractive material for flexible ReRAM because of low temperature growth process [18], [20]. Although the performance of these devices is rather limited till date, the findings suggest a huge potential for improvement through optimization of process parameters as well as by suitable material selection. On the other hand, among the TMOs, HfO_2 is well-recognized as one of the most stable and reliable TMOs for numerous electronics applications including ReRAM applications [22-25]. A very promising approach to improve the device performance could be to combine the advantages of both GO and HfO_2 [26].

In view of the above, here we have reported the improved resistive switching performance of the flexible ReRAM using GO/HfO_x bilayer on an indium tin oxide (ITO) coated polyethylene terephthalate (PET) film. The synthesized material was characterized using electron microscopy, X-ray diffraction (XRD), UV-Vis absorption spectroscopy, X-ray photoelectron spectroscopy (XPS) and Raman spectroscopy whereas the resistive switching performance were characterized by current-voltage (I-V) characteristic. Switching mechanism of the device was explained in terms of migration of oxygen vacancies.

2 Experiment

2.1 Materials

Natural graphite flakes were procured from Kai Yu Industries, Nanjing, China. $NaNO_3$ (≥ 99.5%), $KMnO_4$ (min 99%) and H_2SO_4 (95 – 99%), H_2O_2 (30%) were procured from Merck, India.

2.2 GO Synthesis

GO was synthesized following a modified Hummers' method [27] in which expandable graphite flakes and $NaNO_3$ were first added into concentrated (98%) H_2SO_4 in an ice bath under stirring followed by addition of $KMnO_4$. H_2O_2 was finally added to reduce any residual permanganate and manganese dioxide to colorless and water soluble manganese sulphate. Dried GO in powder form was collected from the golden brownish solution by repeated washing and centrifugation until pH neutral. A solution (0.1 mg/ml) was prepared by dissolving GO in a solution of water and ethanol (1:1).

2.3 Device Fabrication

To fabricate the ReRAM devices, the 130 nm thick ITO coated flexible PET substrate (~127 μm) was first cleaned ultrasonically in acetone, 2-propanol and deionized water. Two sets of devices

Al/GO/ITO/PET (D1) and Al/GO/HfO_x/ITO/PET (D2) were fabricated at room temperature to compare the effect of HfO_x on the switching performance. To prepare the Al/GO/ITO/PET devices, 50 µL of GO solution (0.1 mg/ml) was deposited on the ITO coated PET surface using a spin coater run at 2000 r.p.m (after a particular wetting time of 45 s). For Al/GO/HfO_x/ITO/PET devices, prior to deposition of the GO film (110 nm), a thin layer of HfO_x of 22 nm was deposited on the ITO coated PET substrate by DC sputtering of Hf metallic target (purity – 99.99%) at room temperature in an Ar and O_2 mixed environment with flow ratio of 1:1 while the working pressure in the sputter chamber was maintained at 0.024 mbar. Finally, Al metal dots of diameter in the range of 200-2000 µm were deposited using a hard shadow mask to fabricate the Al/GO/ITO/PET and Al/GO/HfO_x/ITO/PET devices as mentioned in the Table I. The schematic of the final fabricated devices is depicted in Fig. 1.

2.4 Characterization of materials and devices

The thickness of the HfO_x layers was calibrated by spectroscopic ellipsometry measurement of control sample deposited on Si substrate, using an ellipsometer (J. A. Wollam VASE). The surface morphology of GO film and its thickness on the devices were determined by electron microscopy using a Field Emission Scanning Electron Microscope (FESEM) operated at 5 kV accelerating voltage (Zeiss Sigma).

UV-Visible absorption spectrum of GO was recorded in water using a JASCO 750 spectrophotometer. Raman spectrum was recorded by a Raman Spectrometer (LabRAM HR Jobin Yvon) with 532 nm laser and was calibrated using the position of the Si peak at 520 cm^{-1} (not shown here). It confirmed the graphitic structure due to presence of the G band at 1598 cm^{-1} [27], [28]. XPS of GO film was performed using a hemispherical analyser (PSP Vacuum Technology, TX400) using Al Kα source (1486.6 eV) at normal emission. The spectrometer was calibrated

using the Ag $3d_{5/2}$ photoelectron line at a binding energy (BE) of 368.27 eV with a full width at half maximum (FWHM) of 0.8 eV. The binding energies were corrected by setting the position of the C1s peak originating from graphitic carbon at 284.6 eV in accordance with established literature [27], [29]. The XPS data were analysed using CasaXPS software, the peaks were fitted with Gaussian/Lorentzian line shapes and the background was fitted with a Shirley type background subtraction. The atomic ratios have been calculated via XPS measurements by evaluating the area under peak curve values and taking into account the respective sensitivity factors [30]. The electrical measurement of the fabricated devices was carried out using a Keysight B2912A source measure unit. The voltages were applied on the top electrode (Al), while the bottom electrode (ITO) was grounded during the electrical measurements.

3 Result and discussion

3.1 Material characterization

Fig 2 (a) shows a sharp peak corresponding to (002) diffraction planes of GO at 2θ angle 9.44° which is in accordance with an interlayer spacing of 9.36Å and comparable with other reported data [31], [32]. This increase in d-spacing of GO planes compared to that of graphite (3.34 Å) is due to creation of oxygen containing functional groups on graphitic layers that push them away from each other [33]. Fig 2(b) shows the FESEM micrograph of GO powder pressed on a carbon tape in which one can clearly see thin sheet like structures of GO several microns in size and possibly consisting of a few layers. The UV-Visible absorbance spectrum of GO shows a strong absorption at 304 nm (Fig. 2(c)), which indicates the π-π^* transition of the atomic C-C bonds whereas the weaker shoulder peak at 304 nm originates from the n-π^* transition of atomic C-C bonds [31], [34]. Since it is important for an active switching material to exhibit property of insulator at unbiased condition, the band gap of GO was measured using the absorbance data by

Tauc method [35], [36]. Considering that GO exhibits direct allowed transition of electrons across its band gap, the band gap of GO was determined from the intercept of the Tauc plot on the X axis and was found to be 4.2 eV as shown in Fig. 2(d) which is close to the values reported for GO by other groups [31], [37], [38].

The C 1s XPS spectrum is shown in Fig. 3(a) in which it is clear that the C atoms are bound with different oxygen functional groups. The BE peaks attributed to the C of C-O bonds, C=O (Carbonyl) bonds and -COOH (carboxyl) bonds at 286.54 eV, 288.80 eV and 290.97 eV respectively [39]. The intensity ratios of the C-C and C-O components of the C 1s are in accordance with established literatures [40], [41]. XPS was also used to estimate the energy band gap of the GO film by measuring the difference between the positions of the O1s peak from O1s spectrum and the X-axis intercept of a line obtained by extrapolating the linear fit of the onset of the inelastic losses on the lower binding energy side of the main O1s peak (Fig. 3b) in accordance with established literature [42]. Interestingly, the band gap was found to be 4.21 eV in very good agreement with that obtained from UV-absorbance data. Oxygen to carbon ratio (O: C) ratio was found to be 68.52 %. Since, in the literature, there is a strong dependence of the band gap of GO on the relative atomic percentage of oxygen to carbon, we have estimated this value for our GO film to be 68.52 % by quantitative measurement of the XPS survey spectrum. After plotting our experimental data along with the previously reported data [43-45] we have found a linear curve as shown in Fig. 3(c). This experimental data will be helpful to model degree of oxidation of GO from the band gap value. The 22 nm HfO_x film was deposited on the ITO coated PET flexible substrate at room temperature, to check the oxidation state HfO_x using XPS. The Hf 4f core level spectrum was fitted with a spin orbit doublet with splitting of 1.52 eV with an intensity ratio of

(Hf $4f_{7/2}$: Hf $4f_{5/2}$) is 0.75 as expected. The Hf $4f_{7/2}$ CL for has a binding energy of 16.30 eV, which is attributed to nonstoichiometric/oxygen deficient HfO_{2-x} [46], [47].

3.2 Resistive Switching Characterization

The current vs. voltage (I–V) characteristics of Al/GO/ITO/PET (D1) and Al/GO/HfO_x/ITO/PET (D2) devices of diameter 200 μm are shown in Fig. 4. The electrical characterization of devices was carried out by sweeping a continuous voltage of $0 \rightarrow V_{max} \rightarrow 0 \rightarrow -V_{max} \rightarrow 0$. At certain voltages (1.24 V for D1 and 0.90 V for D2), the current increases suddenly and the devices switch from HRS to LRS and a conductive filament was formed. This phenomenon is known as SET process and the device attains the ON state. Even after the removal of the voltage the devices remains in LRS confirming the non-volatility of the devices. When the opposite polarity of the voltage is applied to the devices, the devices switch back from LRS to HRS at –4.06 V and –2.72 V for D1 and D2, respectively through the rupture of the filament. This is known as RESET process, and the devices attain the OFF state. Both the devices show bipolar resistive switching (BRS) behavior. In general, it has also been observed that a higher voltage as compared to SET/RESET voltages is required to the pristine devices to initiate the switching cycle [47]. Here, no initial separate electroforming process is required to initiate the switching cycle which could have been advantageous for low power applications. Similar BRS behavior was previously observed in GO-polyvinylidene difluoride (PVDF) based switching and was attributed to the formation and rupture of oxygen vacancy modulated conduction filament [48].

Fig. 5 presents box plots distribution of cell-to-cell variation of the SET and RESET voltages (V_{SET} and V_{RESET}) and the HRS and LRS currents measured at 0.2 V (I_{HRS} and I_{LRS}) for D1 and D2 devices, respectively. The mean V_{SET}/V_{RESET} voltages are found to be 1.5 V and -4.2 V for D1

devices whereas the mean V_{SET}/V_{RESET} voltages are 1.1 V and –2.8 V for D2 devices. The large variation RESET and HRS current has been observed in Al/GO/ITO/PET (D1) devices mainly due of varied filament dimensions and random rupture process of conductive filament in the GO switching layer [20]. However, the Al/GO/HfO_x/ITO/PET (D2) devices show an improved cell-to-cell variation of SET and RESET voltages as compared to Al/GO/ITO/PET (D1) devices as depicted in Fig. 5(a). The SET/RESET voltages have also significantly been reduced by incorporating a thin HfO_x layer in Al/GO/HfO_x/ITO/PET devices. Similarly, there is a significant reduction of cell-to-cell variation of HRS current in Al/GO/HfO_x/ITO/PET devices, as shown in Fig. 5(b). The higher value of current/resistance ratio between HRS and LRS is observed for D2 bilayer devices with the mean value of 2167. The uniform SET/RESET voltages and higher current/resistance ratio in Al/GO/HfO_x/ITO/PET may be attributed to increasing the oxygen vacancies at GO/HfO_x interface [49]. The interfacial HfO_x acts a reservoir of oxygen vacancies as observed in XPS analysis which result in the formation of uniform conductive filament in the GO layer [50].

Moreover, an elaborate analysis of current voltage relationship of both Al/GO/ITO/PET (D1) and Al/GO/HfO_x/ITO/PET (D2) ReRAM devices is carried out to find out the conduction mechanism. The I-V curves are replotted in double logarithmic scale for both D1 and D2 as shown in Fig. 6. It clearly exhibits that LRS is dominated by Ohmic conduction behavior for both D1 and D2 devices with slope ~ 1. The Ohmic behaviour in the LRS state has usually been attributed to the formation of conductive filaments in switching oxide layers during the SET process [18], [21], [51]. However, the conduction mechanism in HRS is much more complicated. The fitted results of I-V curves for HRS in SET cycle consists of an Ohmic region ($I \propto V$) with slope ~ 1 and Child's law region ($I \propto V^2$) with slope 1.8 and 2.1 for D1 and D2, respectively. This conduction mechanism

can be explained in terms of trap-controlled space charge limited conduction (SCLC) [10], [18], [21], [51-53], where oxygen vacancies present in the GO single layer or GO/HfO_x bilayer act as traps for the electrons. Similarly, fitted I-V curves for the negative RESET cycle, LRS follows the Ohmic behaviour and the HRS follows the trap controlled SCLC mechanism.

According to the above experimental results, the possible switching mechanism in the bilayer Al/GO/HfO_x/ITO/PET ReRAM can be explained by the oxygen vacancies migration-induced oxidation/reduction reaction at the interface of GO/HfO_x, as schematically shown in Fig. 7. When a positive voltage is applied at Al top electrode, the oxygen ion (O^{2-}) ions move upwards leaving the oxygen vacancies in GO layer and the bottom HfO_x also acts a source of oxygen vacancies. In addition, the top electrode Al as an oxygen scavenging layer may enhance the oxygen vacancies in the GO layer [54]. These vacancies form an oxygen deficient filament which is conducting in nature and the device switches from the HRS to the LRS. When negative bias voltage is applied on the top electrode, oxygen ions migrate towards the bottom electrode and recombine with oxygen vacancies in HfO_x layer by Joule heating generated in LRS, leading to the disruption of the conductive filament and the device switches from LRS to HRS. As the HfO_x provides more oxygen vacancies, it may act as a virtual cathode to assist the formation of the uniform conductive path at lower SET voltage as compared to the Al/GO/ITO/PET devices. The RESET process is described as a field and Joule heating assisted diffusion process of oxygen ions and vacancies, leading to the rupture of the conducting filament [55]. As the LRS current is higher in Al/GO/HfO_x/ITO/PET devices as observed earlier, the higher Joule heating will trigger the ionic migration more to rupture the conductive filament at lower RESET voltage as compared to the Al/GO/ITO/PET devices.

Fig. 8(a) shows the retention characteristics of Al/GO/HfO_x/ITO/PET flexible ReRAM device at room temperature. There is no degradation of resistance ratio between LRS and HRS till 10^3 s at room temperature. The excellent retention of the Al/GO/HfO_x/ITO/PET device is attributed to the presence of more oxygen vacancies in the GO layer assisted by the bottom HfO_x layer [50]. The resistive switching behaviour of Al/GO/HfO_x/ITO/PET ReRAM has been measured under the different bending radii for flexible application. Fig 8 (b) shows the variation of LRS and HRS resistances measured at 0.2V as a function of bending radii. There is a slightly decreasing tendency of $R_{LRS/HRS}$ resistance values at the bending radius down to 5 mm from flat (15 mm) condition, indicating a stable and sufficient LRS/HRS ratio of the GO/HfO_x flexible memory device. The decrease of the memory window may be due to the cracks developed in the ITO bottom electrode under extremely flexed condition [10], [26].

Table II enlists some of the recently reported flexible GO-Based ReRAMs with organic, inorganic, and perovskite active layers and associated parameters such as switching voltages, switching currents, switching power and memory window. In this study, the switching power is determined at the switching point where the devices change their state from HRS to LRS and vice-versa. The present Al/GO/HfO_x/ITO/PET device shows lower switching voltages and higher resistance ratio with minimum cell to cell variation.

4 Conclusion

In this work, the improved resistive switching characteristics have been observed in Al/GO/HfO_x/ITO/PET flexible ReRAM devices by incorporating a thin HfO_x layer. With the help

of FESEM, UV-Spectroscopy, XRD and XPS material properties of the graphene oxide and HfO_x films are investigated. The presence of different oxygen functional group (carboxyl group, carbonyl group) is confirmed by XPS analysis. The band gap of GO is found to be 4.21 eV with O:C ratio of 68.52%. The ReRAM devices exhibit the forming free, bipolar resistive switching characteristics. The existence of HfO_x layer may enhance the control of the O-deficiency level in the GO layer which shows the stable, uniform and improved bipolar resistive switching behavior. The devices show excellent resistive switching properties at room temperature with sufficient memory window $>10^3$, high retention and low operating voltages. Investigation of conduction mechanisms of HRS and LRS confirms that bipolar resistive switching in HRS and LRS is dominated by SCLC mechanism and Ohmic, respectively.

Acknowledgement

This work is supported in part by the DST SERB project, Govt of India, Ref no: EMR/2016/006814. A. D. Paul acknowledges the UGC NET JRF fellowship for supporting the PhD research work. AKC acknowledges the MHRD (TEQIP-III) funded Centre of Excellence in Advanced Materials at NIT Durgapur for some of the characterizations.

Declarations:

Funding: This work is supported in part by the DST SERB project, Govt of India, Ref no: EMR/2016/006814. A. D. Paul acknowledges the UGC NET JRF fellowship for supporting the

PhD research work. AKC acknowledges the MHRD (TEQIP-III) funded Centre of Excellence in Advanced Materials at NIT Durgapur for some of the characterizations.

Conflicts of interest/Competing interests: There is no conflict of interest.

Availability of data (data transparency): Available on request

Code availability (software application or custom code): Not Applicable

References

[1] L. Zhou, J. Mao, Y. Ren, S.-T. Han, V. A. L. Roy, and Y. Zhou, Small 1703126 (2018).

[2] M. T. Ghoneim and M. M. Hussain, Electronics 4, 424-479 (2015).

[3] Y. Gu, T. Zhang, H. Chen, F. Wang, Y. Pu, C. Gao, and S. Li, Nanoscale Res. Lett. 14, 263 (2019).

[4] S. Maikap, and W. Banerjee, Adv. Electron. Mat, 2000209 (2020)

[5] R. Waser, R. Dittmann, G. Staikov, and K. Szot, Adv. Mater. 21, 2632–2663 (2009).

[6] S. Samanta, X. Gong, P. Zhang, K. Han, and X. Fong, J. Alloys Compounds, 805, 915–923, (2019).

[7] W. Banerjee, Electronics 9, 1029 (2020).

[8] R.-C. Fang, Q.-Q. Sun, P. Zhou, W. Yang, P.-F. Wang, and D. W. Zhang, Nanoscale Res. Lett. 8, 92 (2013).

[9] L. Gong, Y.-Z. Liu, F.-Y. Liu, and L.-X. Jiang, J Mater Sci: Mater Electron 28, 6093–6098 (2017).

[10] A. D. Paul, S. Biswas, P. Das, H. J. Edwards, V. R. Dhanak, and R. Mahapatra, IEEE Trans. on Electron Devices 67, 4222-4227, (2020).

[11] M.-J Lee,S. Han, S. H. Jeon, B. H. Park, B. S. Kang, S.-E. Ahn, K. H. Kim, C. B. Lee,C. J. Kim, I.-K. Yoo, D. H. Seo, X.-S. Li, J.-B. Park, J.-H. Lee, and Y. Park, Nano Lett. 9, 1476–1481 (2009).

[12] J. J. Yang, F. Miao, M. D. Pickett, D. A. A. Ohlberg, D. R. Stewart, C. N. Lau, and R. S. Williams, Nanotechnol. 20, 215201 (2009).

[13] Y. C. Yang, F. Pan, Q. Liu, M. Liu, and F. Zeng, Nano Lett. 9, 1636–1643 (2009).

[14] K. Szot, W. Speier, G Bihlmayer, and R. Waser, Nat. Mater. 5, 312–320 (2006).

[15] J. Ouyang, C.-W. Chu, C. R.Szmanda, L. Ma, and Y. Yang, Nat. Mater. 3, 918–922 (2004).

[16] S. K. Hwang, J. M. Lee, S. Kim, J. S. Park, H. I. Park, C. W. Ahn, K. J. Lee, T. Lee, and S. O. Kim, Nano Lett. 12, 2217−2221 (2012).

[17] Z. Wu, X. Zhao, Y. Yang, W. Wang, X. Zhang, R. Wang, R. Cao, Q. Liuac, and W. Banerjee, Nanoscale Adv. 1, 3753–3760 (2019).

[18] L.-H. Wang, W. Yang, Q.-Q. Sun, P. Zhou, H.-L. Lu, S.-J. Ding, and D. W. Zhang, Appl. Phys. Lett. 100, 3–7 (2012).

[19] F. Hui, E. G-. Gutierrez, S. Long, Q. Liu, A. K. Ott, A. C. Ferrari, and M. Lanza, Adv. Electron. Mater. 3, 1600195 (2017).

[20] H. Y. Jeong, J. Y. Kim, J. W. Kim, J. O. Hwang, J.-E. Kim, J. Y. Lee, T. H. Yoon, B. J. Cho, S. O. Kim, R. S. Ruoff, and S.-Y. Choi, Nano Lett. 10, 4381-4386 (2010).

[21] A. Midya, N. Gogurla, and S. K. Ray, Curr. Appl. Phys 15, 3902 (2015).

[22] R. Mahapatra, Amit K. Chakraborty, A. B. Horsfall, S. Chattopadhyay, N. G. Wright, and Karl S. Coleman, J. Appl. Phys 102, 024105 (2007).

[23] R. Mahapatra, Amit K. Chakraborty, A. B. Horsfall, N. G. Wright, G. Beamson, Appl. Phys. Lett. 92, 042904 (2008).

[24] M. Yuan, Y.-T. Tseng, P.-H. Chen, C.-C. Shih, H.-C. Huang, T.-C. Chang, X. Cui, X. Lin, S. Zhang, and H. Zhou, J. Electron Devices Soc. 6, 627-632 (2018).

[25] R. Mahapatra, S. Maji, A.B. Horsfall, and N.G. Wright, Microelectron. Eng. 138, 118–121 (2015).

[26] V. K. Nagareddy, M. D. Barnes, F. Zipoli, K. T. Lai, A. M. Alexeev, M. F. Craciun, and C. D. Wright, ACS Nano 11, 3010−3021 (2017).

[27] S. Chakraborty, S. Saha, V. R. Dhanak, K. Biswas, M. Barbezat, G. P. Terrasid, and A. K. Chakraborty, RSC Adv. 6, 67916-67924 (2016).

[28] A. K. Chakraborty and K. S. Coleman, J. Nanosci. Nanotechnol. 8, 4013–4016 (2008).

[29] A. K. Chakraborty, R.A.J. Woolley, Y. V. Butenko , V. R. Dhanak, L. S iller, and M. R. C. Hunt, Carbon 45, 2744–2750 (2007).

[30] J. F. Moulder, W. F. Stickle, P. E. Sobol, and K. D. Bomben, Physical Electronics Inc., USA, 1993.

[31] V. Meriga, S. Valligatla, S. Sundaresan, C. Cahill, V. R. Dhanak, A. K. Chakraborty, J. Appl. Polym. Sci. 132 , 42766 (2015).

[32] I. Banerjee, P. Harris, A. Salimian, and A. K. Ray, IET Circuits Devices Syst. 9, 428–433 (2015).

[33] W. Zhao, G. Kido, S. Harada, M. Unno, H. Noguchi, J. Colloid Interface Sci 431, 8–16 (2014).

[34] J. Yang and S. Gunasekaran, Carbon, 51, 36-44 (2013).

[35] J. Tauc, Mater. Res. Bull. 3, 37–46 (1968).

[36] R. K. Agrawalla, V. Meriga, R. Paul, A. K. Chakraborty, and A. K. Mitra, Expr. Polym. Lett. 10, 780-787 (2016).

[37] H.-C. Hsu, I. Shown, H.-Y. Wei, Y.-C. Chang, H.-Y. Du,Y.-G. Lin, C.-A. Tseng, C.-H. Wang, L.-C. Chen, Y-C.Lindand, K.-H. Chen, Nanoscale 5, 262–268 (2013).

[38] P. Kumar, A. Bansiwal, N. Labhsetwarb, and S. L. Jain, Green Chem.17, 1605 (2015).

[39] R. Maiti, S. Manna, A. Midya, and S. K. Ray, Opt. Express 21, 26034-26043 (2013).

[40] H. F. Liang, C. T. G. Smith, C. A. Mills, and S. R. P. Silvab, J. Mater. Chem. C **3**, 12484-12491 (2015).

[41] P. Ranjan, S. Agrawal, A. Sinha, T. R. Rao, J. Balakrishnan, and A. D. Thakur, Sci Rep 8, 12007 (2018).

[42] P. Das, L. A. H. Jones, J. T. Gibbon, V. R. Dhanak, T. P. -Manzanera, J. W. Roberts, R. Potter, P. R. Chalker, S.-J. Cho, I. G. Thayne, R. Mahapatra, and I. Z. Mitrovic, ECS J. Solid State Sci. Technol. 9, 063003 (2020).

[43] H. Huang, Z. Li, J. She, and W. Wang, J. Appl. Phys. 111, 054317 (2012).

[44] V. Gupta, N. Sharmab, U. Singh, M. Arif, and A. Singh, Optik 143, 115–124 (2017).

[45] M. Lundie, Z. Sljivancanin, and S. Tomic, TMCSIV 526, 012003 (2014).

[46] S. U. Sharath, T. Bertaud, J. Kurian, E. Hildebrandt, C. Walczyk, P. Calka, P. Zaumseil, M. Sowinska, D.Walczyk, A. Gloskovskii, T. Schroeder, and L. Alff, Appl. Phys. Lett. 104, 063502 (2014).

[47] S. Maji, S. Samanta, P. Das, S. Maikap, V. R. Dhanak, I. Z. Mitrovic, and R. Mahapatra, J. Vac. Sci. Technol. B 37, 021204 (2019).

[48] A. Thakre and A. Kumar, J. Alloys Compd.722,579-584(2017).

[49] S. Choudhary, M. Soni, and S. K. Sharma, Semicond. Sci. Technol. 34, 085009 (2019).

[50] R. Zhang, H. Huang, Q. Xia, C. Ye, X. Wei, J. Wang, L. Zhang, and L. Q. Zhu, Adv. Electron. Mater. 5, 1800833 (2019).

[51] T. Liu, W. Wua, N. K. Liao, Q. Sun, X. Gonga, V. A. L Roy, Z. Z. Yu, and R. K. Y.Li, Carbohydrate Polymers 214, 213–220 (2019).

[52] S. K. Hong, J. E. Kim, S. O. Kim, and B. J. Cho, J. Appl. Phys. 110, 044506 (2011).

[53] S. Chakrabarti, S. Samanta, S. Maikap, S. Z. Rahaman, and H.-M. Cheng, Nanoscale Res. Lett. 11, 389 (2016).

[54] M. K. Hota, C. Mukherjee, T. Das, and C. K. Maiti, ECS J. Solid State Sci. Technol. 1, N149–N15 (2012).

[55] X. Zhang, L. Xu, H. Zhang, J. Liu, D. Tan, L. Chen, Z. Ma, and W. Li, Nanoscale Res. Lett. 15, 11 (2020).

[56] G. Khurana, P. Misra, N. Kumar, and R. S. Katiyar, J. Phys. Chem. C 118, 21357−21364 (2014).

[57] H. Tian, H.-Y. Chen, T.-L. Ren, C. Li, Q.-T. Xue, M. A. Mohammad, C. Wu, Y. Yang, and H.-S. P. Wong, Nano Lett. 14, 3214−3219 (2014).

[58] M. M. Rehman, G. U. Siddiqui, S. Kim, and K. H. Choi, J. Phys. D: Appl. Phys. 50, 335104 (2017).

Figure Captions:

Fig. 1 Schematic diagram of (a) Al/GO/ITO/PET (D1) and (b) Al/GO/HfO_x/ITO/PET (D2) devices.

Fig. 2 (a) XRD pattern of GO sample (b) FESEM image of GO powder sample (c) UV-visible absorbance spectrum of GO sample (d) Tauc plot of $(\alpha h\nu)^2$ against incident photon energy $h\nu$

Fig. 3 X-ray photoelectron spectra of (a) Deconvoluted C1s of GO (b) O 1s Loss spectroscopy for band gap estimation (c) O/C atomic percentage versus band gap (d) Hf 4f core level for HfO_x layer.

Fig. 4 Current vs. voltage (I–V) characteristics of Al/GO/ITO/PET (D1) and Al/GO/HfO_x/ITO/PET (D2) devices. The arrows in the graphs indicate the switching direction.

Fig. 5 Box plot distribution of (a) SET and RESET voltages (b) LRS and HRS currents of D1 and D2 devices. All are read at 0.2V.

Fig. 6 Double-logarithmic plot of I-V characteristics of D1 and D2 ReRAM devices for (a) positive and (b) negative cycle, respectively.

Fig. 7 Schematic switching mechanism of Al/GO/HfO_x/ITO/PET ReRAM under (a) positive bias and (b) negative bias.

Fig. 8 (a) The retention characteristics of the HRS and the LRS at room temperature with the On/Off ratio up to 10^3 s. (b) The variation of LRS and HRS resistance as function of bending radii of the Al/GO/HfO_x/ITO/PET flexible ReRAM

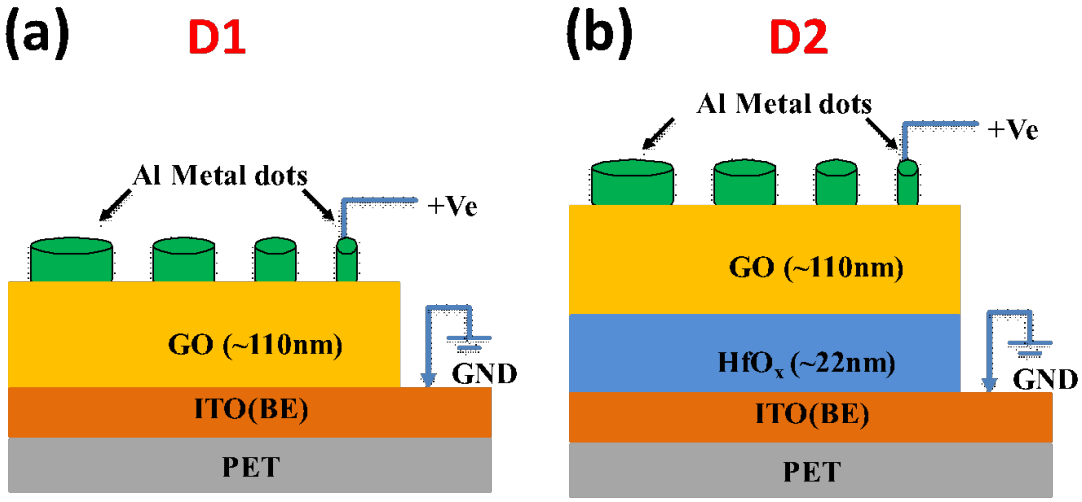
(a)
D1
Al Metal dots
+Ve
GO (~110nm)
GND
ITO(BE)
PET
(b)
D2
Al Metal dots
+Ve
GO (~110nm)
HfO$_x$ (~22nm)
GND
ITO(BE)
PET

Fig. 1

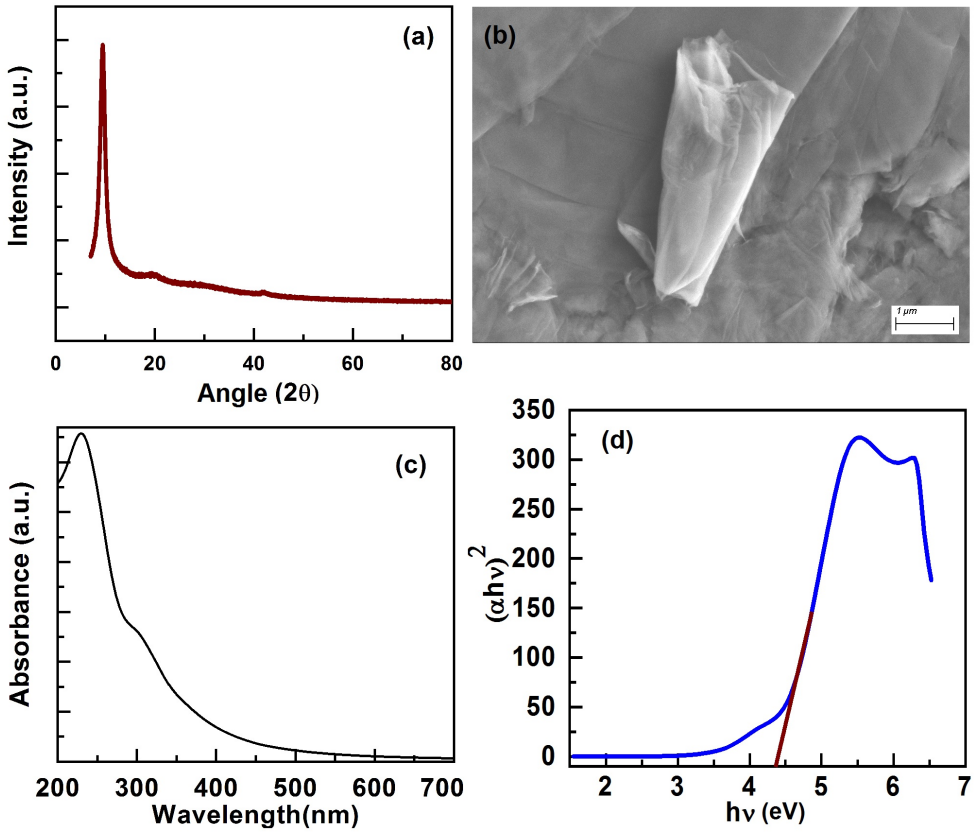
(a)
Intensity (a.u.)
0
20
40
60
80
Angle (2θ)
(b)
1 μm
(c)
Absorbance (a.u.)
200
300
400
500
600
700
Wavelength(nm)
(d)
(αhν)2
350
300
250
200
150
100
50
0
2
3
4
5
6
7
hν (eV)

Fig 2

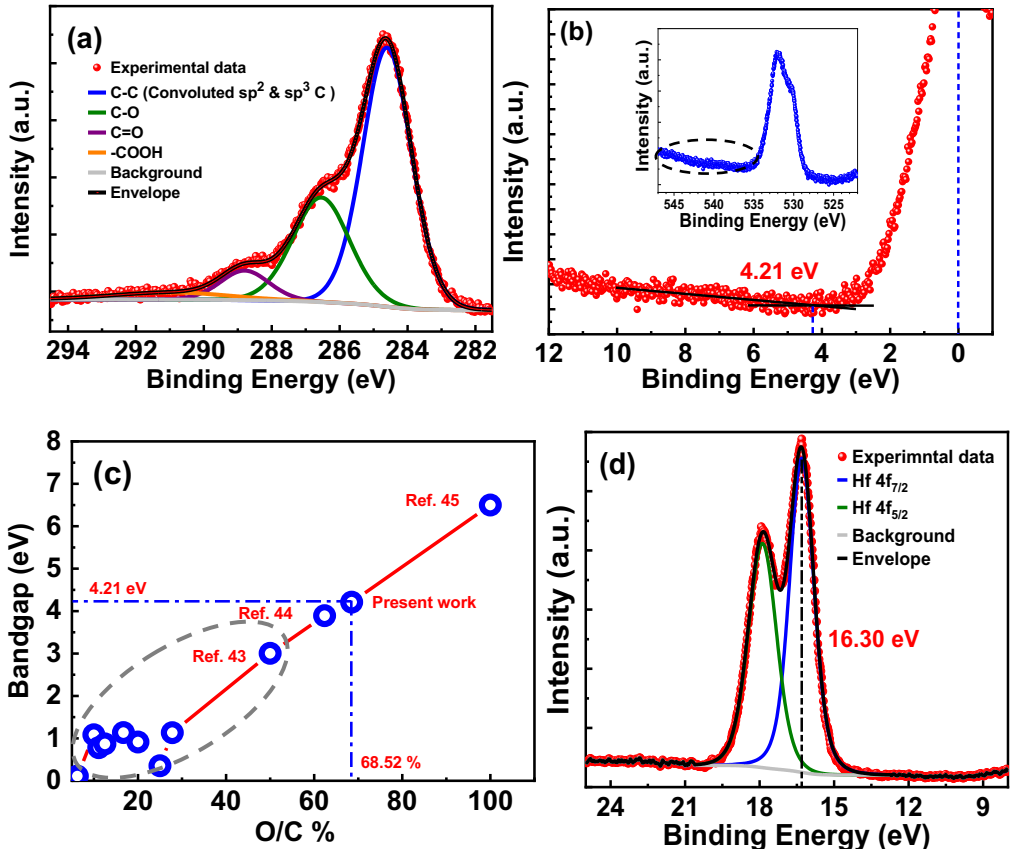
(a)
Experimental data
C-C (Convoluted sp2 & sp3 C)
C-O
C=O
-COOH
Background
Envelope
Intensity (a.u.)
294 292 290 288 286 284 282
Binding Energy (eV)
(b)
Intensity (a.u.)
545 540 535 530 525
Binding Energy (eV)
4.21 eV
12 10 8 6 4 2 0
Binding Energy (eV)
(c)
Bandgap (eV)
0 1 2 3 4 5 6 7 8
Ref. 45
4.21 eV
Present work
Ref. 44
Ref. 43
68.52 %
20 40 60 80 100
O/C %
(d)
Experimntal data
Hf 4f7/2
Hf 4f5/2
Background
Envelope
16.30 eV
Intensity (a.u.)
24 21 18 15 12 9
Binding Energy (eV)

Fig. 3

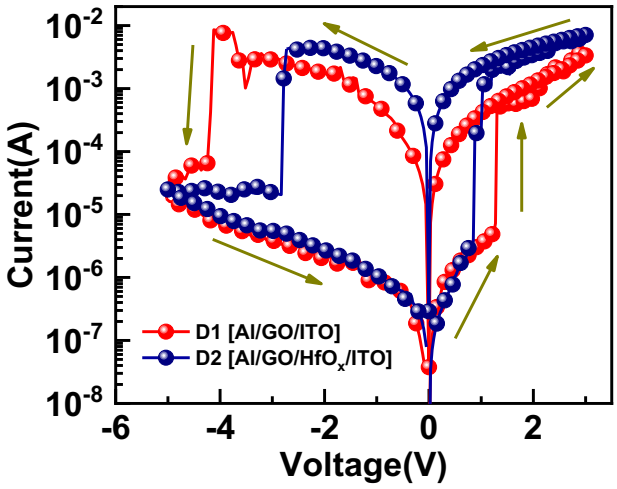
Current(A)
10-2
10-3
10-4
10-5
10-6
10-7
10-8
-6
-4
-2
0
2
Voltage(V)
D1 [Al/GO/ITO]
D2 [Al/GO/HfOx/ITO]

Fig. 4

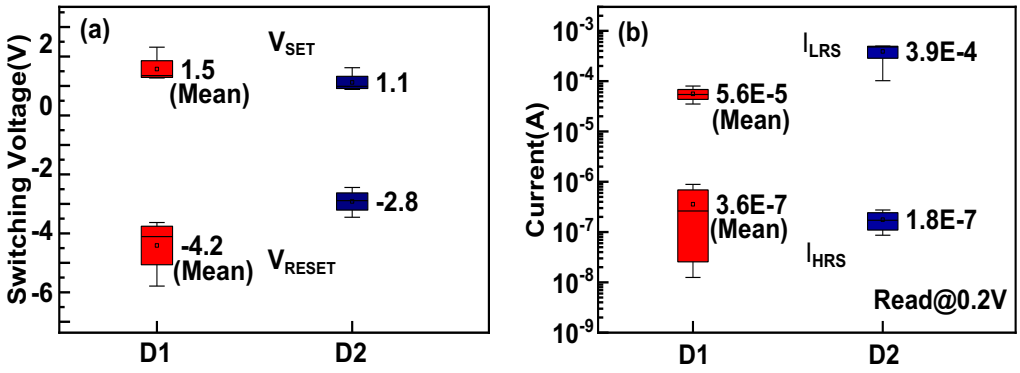
(a)
Switching Voltage(V)
2
0
-2
-4
-6
V_SET
1.5
(Mean)
1.1
-2.8
-4.2
(Mean)
V_RESET
D1
D2
(b)
Current(A)
10^-3
10^-4
10^-5
10^-6
10^-7
10^-8
10^-9
I_LRS
3.9E-4
5.6E-5
(Mean)
3.6E-7
(Mean)
1.8E-7
I_HRS
Read@0.2V
D1
D2

Fig. 5

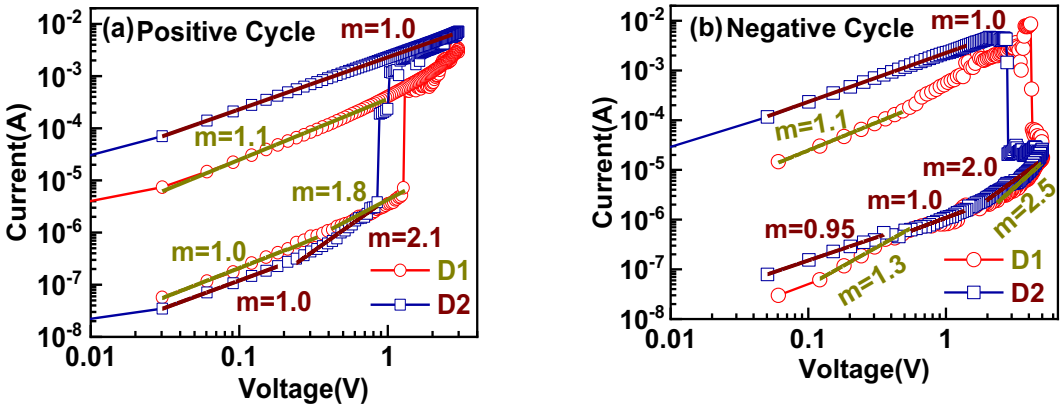
(a) Positive Cycle
m=1.0
m=1.1
m=1.8
m=2.1
m=1.0
m=1.0
D1
D2
Current(A)
Voltage(V)
(b) Negative Cycle
m=1.0
m=1.1
m=2.0
m=1.0
m=0.95
m=2.5
m=1.3
D1
D2
Current(A)
Voltage(V)

Fig. 6

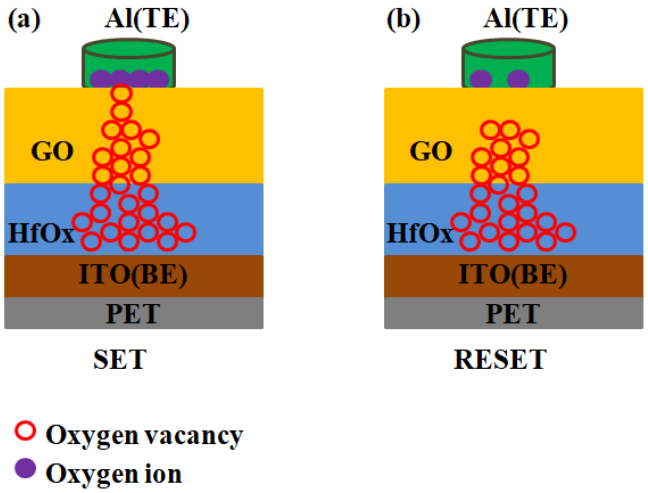
(a)
Al(TE)
GO
HfOx
ITO(BE)
PET
SET
(b)
Al(TE)
GO
HfOx
ITO(BE)
PET
RESET
Oxygen vacancy
Oxygen ion

Fig. 7

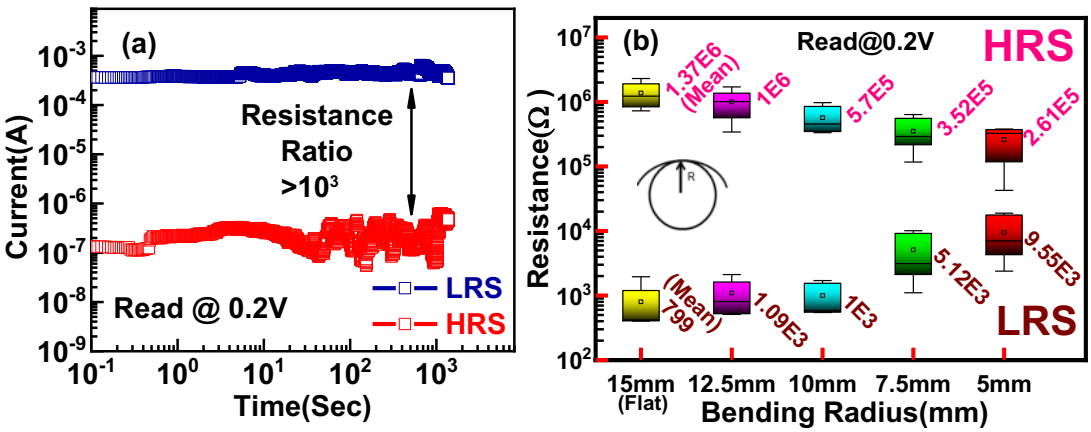
(a)
Resistance
Ratio
>10³
Read @ 0.2V
LRS
HRS
Current(A)
Time(Sec)
(b)
Read@0.2V
HRS
LRS
Resistance(Ω)
1.37E6
(Mean)
1E6
5.7E5
3.52E5
2.61E5
(Mean)
799
1.09E3
1E3
5.12E3
9.55E3
15mm
(Flat)
12.5mm
10mm
7.5mm
5mm
Bending Radius(mm)

Fig. 8

Table Caption:

Table 1 List of Fabricated devices in this study.

Device name	Device Structure	Active layer Thickness
D1	Al/GO/ITO/PET	GO (~ 110nm)
D2	Al/GO/HfO_x/ITO/PET	GO (~110nm)/HfO_x(22nm)

Table 2 Performance comparison of some recently reported GO-Based flexible RRAMs.

Dielectric layer	Top Electrode	Bottom Electrode	Substrate	V_{SET}/V_{RESET}	I_{SET} and I_{RESET}	P_{SET}/P_{RESET}	Memory Window	Ref.
GO/HfOx	**Al**	**ITO**	**PET**	**1.1V / -2.8V**	**~ 3×10^{-3} A/3×10^{-3} A**	**3.3mW/ 8.4mW**	**2167**	**This Work**
GO	Al	ITO	PET	2.2V / -3.5V	10^{-3}A / 2×10^{-3}A	2.2mW/ 7mW	280	[18]
GO	Al	Al	PES	–2.5V / 2.5V	2×10^{-5}A / 9×10^{-6}A	50μW/ 22.5 μW	>100	[20]
RGO	Al	ITO	PET	-5.6V / 3.9V	~10^{-5} A	56 μW/ 39μW	>10^2	[21]
GO/TiO_2	Ti/Pt	Ti/Pt	PEN	-3.2V / 3.3V	~ 8×10^{-3} A	~26mW	~100	[26]
CMC-GO	Al	Al	PET	2.2V / NA	~10^{-2} A	22mW/ NA	>10^3	[51]
GO:ZNs	Al	ITO	PET	2.1V / -2V	2×10^{-3}A / 3×10^{-3}A	4.3mW/ 6mW	~100	[56]
HfO_x	Ag	laser-scribed rGO (LSG)	PET	1.4V / -3V	~10^{-4} A	0.14mW/ 0.3mW	~10	[57]
GQD–hBN	Ag	Ag	PET	~4V / -4V	~10^{-4} A	~0.4mW	>10^3	[58]